The dependence of the proton-triton thermo-nuclear fusion reaction rate
on the temperature and total energy content
of the high-energy proton distribution function

D.Testa[1], M.Cecconello[2], C.Schlatter[1], and JET-EFDA contributors[*]

[1] CRPP, Association EURATOM – Confédération Suisse, EPFL, Lausanne, Suisse

[2] Division of Fusion Plasma Physics (Association EURATOM/VR), Alfvén Laboratory, Royal Institute of Technology, Stockholm, Sweden

The endothermic nuclear reaction between thermal tritons and high energy protons can represent an important contribution to the total neutron yield in tokamak plasmas heated by radio-frequency waves, as the first JET experiments have demonstrated [*M.Mantsinen et al., Nucl. Fusion **41** (2001), 1815*]. A further study based on more recent JET experiments was reported in [*M.Santala et al., Plasma Phys. Control. Fusion **48** (2006), 1233*]. In this Letter we supplement and complete the previous analysis by reporting the first systematic measurement of the scaling of the proton-triton (pT) thermo-nuclear fusion reaction rate as a function of the total energy content and perpendicular tail temperature of the fast protons heated by radio-frequency waves. It is found that the pT neutron rate increases almost linearly with the fast proton temperature and the total energy content.

PACS numbers: 52.35-g, 52.55.Fa

---

[*] See annex 1 of J.Pamela et al., "*Overview of Recent JET Results*", OV-1/1, IAEA Fusion Energy Conference 2004, *Nucl. Fusion* **45** (2005), S63-S85.

One of the nuclear reactions that can give rise to a significant source of neutrons in fusion plasmas is the endothermic $T(p,n)^3He$ one [1][1]: $T+p+764keV \rightarrow n+^3He$. This proton-triton (pT) thermo-nuclear fusion reaction requires a proton with energy in excess of $E_{pCM}=764keV$ in the centre-of-mass reference frame. The detailed kinematics of the pT neutron production has been described in [2]. The high energy protons required for the pT fusion are produced in the JET tokamak [3] via Ion Cyclotron Radio Frequency (ICRF) heating of the background minority hydrogen population. Due to broad energy range of the fast protons produced by ICRF heating, the pT neutrons have also a very broad energy spectrum, each neutron being produced at the energy $E_n=0.75\times(E_{pCM}-764keV)$. As shown in fig1 (extracted from [4]), for proton energies $E_{pCM}>2MeV$, this reaction has by far the highest cross-section between those typically occurring in magnetically confined thermo-nuclear fusion plasmas, i.e. those involving hydrogen isotope ions [1].

The interest in studying the pT thermo-nuclear fusion reaction stems from the fact that a background hydrogen population is an unavoidable feature of tokamak plasmas with a first wall covered with carbon tiles, due to the structural properties of the CFC material [5]. In ITER, ICRF heating of the deuterium population is essentially considered as a tool to increase the ion temperature on the road to ignition [5]. However, the presence of a minority hydrogen population will also contribute to the total neutron rate through the pT nuclear reaction, and this needs to be properly considered when evaluating the various neutron production mechanisms as a tool to assess the plasma performance or infer background and fast ion plasma parameters such as the ion temperature and toroidal rotation [6-8]. Furthermore, the pT nuclear reaction has also been tentatively proposed as a possible tool for measuring the temperature of ICRF-driven protons in energy ranges where conventional methods, such as neutral particle analysis or γ-rays spectroscopy, are not available [2]. Hence it is important to derive a scaling for the pT neutron rate R_{pT} as function of the main features of the distribution function of the ICRF-driven high-energy protons $f_{pFAST}(E)$, such as their perpendicular tail temperature $T_{\perp pFAST}$ and total energy content W_{pFAST}.

The first JET experiments have demonstrated the role of the pT nuclear reaction during ICRF heating of the minority proton distribution function in tritium-rich plasmas, $n_T/n_e \approx 0.9$ [10]. However, at that time it had not been possible to perform a systematic scan of the dependence of the pT neutron yield on $f_{pFAST}(E)$. A more systematic experimental study of the pT-neutrons in purely ICRF-heated plasmas with low tritium density (typically $n_T/n_e<0.01$) was performed in 2003 in JET during the Trace Tritium Experiments (TTE) [10, 11], with the main results reported in [2]. Here we supplement the analysis of

---

[1] see also http://www-nds.iaea.org/ for table reporting data on the endothermic fusion reaction $T(p,n)^3He$.

Ref.[2] by concentrating on the scaling of the *excess pT-neutron rate* R_{pT} as function of the core fast proton perpendicular temperature $T_{\perp pFAST,0}$ and total energy content W_{pFAST} in such plasmas.

The excess pT-neutron rate $R_{pT}(t)$ is defined as $R_{pT}=R_{TOT}-(R_{DT}+R_{DD})-R_{ADD}$, where R_{TOT} is the total (measured) neutron rate, R_{DT} is the (measured) 14MeV neutron rate from the DT fusion reactions, R_{DD} is the (measured) 2.5MeV neutron rate from the DD fusion reactions, and R_{ADD} indicates possible (computed/measured) additional sources of neutrons in the energy range of the JET neutron detectors. Examples of possible contributions to R_{ADD} have been described in Ref.[2], and these could introduce a large error in the inferred R_{pT}. However, as the background plasma parameters are almost constant over the various discharges that constitute our database, this error would only be of a systematic nature, hence by its very nature of no consequence for establishing the scaling laws which are the purpose of our experimental work. This is further demonstrated in a later section of this Letter.

Different detectors with often different time resolution were used to obtain the individually calibrated data R_{TOT}, R_{DT} and R_{DD} for the TTE experiments considered here. The total neutron rate R_{TOT} was measured with three sets of fission chambers located around the Torus. Each set comprises a U^{235} and a U^{238} chamber operating in pulse-counting and current mode. The 2.5MeV neutron emission R_{DD} was determined by the *neutron profile monitor* equipped with NE213 liquid scintillators and pulse shape discrimination hardware. Only neutron events within the energy range 1.8÷3.5MeV were detected, and a background subtraction was performed to eliminate events associated with higher energy neutrons (for instance, 14MeV DT-neutrons) that had slowed down, possibly due to scattering in the instrument itself. Two independent measurements of R_{DT} were performed: with silicon diodes, using the threshold reactions Si(n,p) and Si(n,α), applied routinely at JET as 14MeV neutron monitor; and with the newly installed Bicron scintillators, sensitive only to neutrons with $E_n>9$MeV, within the *neutron profile monitor* diagnostic system. A comprehensive and detailed overview of the various neutron diagnostics employed during the TTE experiments in JET is given in Refs.[12-17] and the references therein.

In order to combine the data coming from the different neutron detectors used for these experiments, hence deduce $R_{pT}(t)$, we have devised the procedure described below, which relies upon Gaussian propagation of the errors to track as accurately as possible the time evolution of the uncertainty on the computed $R_{pT}(t)$. First, we have integrated the calibrated data from each individual neutron detector over the longest time window between them all (typically 0.1s÷0.3s depending on the neutron counts) that was necessary to reduce the relative statistical error on each detector measurement (indicated by the subscript "NX") to less than $\sigma_{NX}<10\%$. Such error σ_{NX} was evaluated using the Poisson statistics on the neutron count: $\sigma=1/\sqrt{N}$, N being the total neutron count in the chosen time interval. Second, we

have resampled these data over a 50ms-long time base (i.e., the typical time resolution of the $T_{\perp pFAST}$ measurements) using linear fitting routines for the steady-state phase of the discharge. This time base is now common to all neutron detectors. The error on each resulting time point was then determined by adding the 10% base error to the normalised ratio of the difference between the total neutron count on the short time interval (C_{50ms}) to the expectation value (C_{EXP}) which was obtained from averaging over the long time interval: $\sigma_{NX}=[0.01+(C_{50ms}-C_{EXP})^2/C_{EXP}^2]^{1/2}$. As a practical example to clarify this error propagation process, for an "original" 150ms-long time window used to obtain $\sigma_{NX}<10\%$, with the total neutron count over the 150ms-long time window C_{TOT}, we have $C_{EXP}=C_{TOT}/3$. Third, we supplemented this steady-state analysis for transients such as the ICRF heating switch-on/off phases using guidance from available modelling for a set of similar discharges, such as that provided by the JETTO [18] and TRANSP [19] codes. This approach is useful to determine an empirical dependence of $R_{DD}(t)$ and $R_{DT}(t)$ during these transients as function of various plasma parameters such as the ion temperature, density, heating power and effective charge. This showed that the expected 2.5MeV DD neutron rate with ICRF-only heating and low ion temperature $T_i<10keV$ scales linearly with the ICRF heating power P_{RF}, $R_{DD}\propto n_e^2*P_{RF}/Z_{EFF}$, where n_e is the electron density and Z_{EFF} is the effective charge. On the other hand, the 14MeV DT neutron rate depends essentially on n_T and on the presence of supra-thermal deuterons, as those obtained via Neutral Beam Injection (NBI): $R_{DT}(t)\propto n_e n_T*P_{NBI}/Z_{EFF}$, where P_{NBI} is the NBI power. Therefore, to simplify our analysis, we have decided to ignore the NBI heating phase of all the discharges considered here, including a 300ms time window after the NBI switch-off to allow for the slowing-down of the high-energy NBI deuterons. Over this phase, we have therefore set $R_{pT}=0$ by default. We also note that R_{pT} is typically very low at the start (end) of the ICRF heating phase, before (after) a steady-state $f_{pFAST}(E)$ is established (has decayed) over a few fast proton slowing-down times. Therefore even large statistical errors on the analysis of these transients do not actually affect the overall scaling derived here, for which the bulk of the data is obtained during steady-state phases.

It is also important to point out here that, due to the lack of accurate time-resolved measurement of the tritium concentration, we assumed a constant n_T/n_e, averaged over the steady-state ICRF heating phase of each individual discharge. Hence, n_T was separately estimated by (a) time-integrating the tritium gas puff, (b) using the results of the JETTO and TRANSP simulations (when available), and (c) using the "operational" formula $n_T/n_D\approx R_{DT}/(R_{TOT}-R_{DT})/300$, which was used throughout the TTE experimental campaign to estimate the tritium concentration from the 14MeV neutron rate for an estimated ion temperature $T_i=10keV$. Note that $T_i(keV)\approx3\div5$ for the experiments reported here, therefore the estimate (c) is in principle inaccurate, and it is mainly used here to provide a further constraint on the ratio n_T/n_D.

The value of n_T/n_e used in the analysis reported here comes from the averaging over the duration of the ICRF heating phase of these separate estimates, thus adding the further source of uncertainty σ_{nT} to the calculation of $R_{pT}(t)$. The total relative statistical error on $R_{pT}(t)$ was therefore empirically determined as $\sigma_{RPT}=[\sigma_{RTOT}{}^2+\sigma_{RDD}{}^2+\sigma_{RDT}{}^2+\sigma_{nT}{}^2]^{1/2}$.

It is important to note here that the total neutron rate diagnostic (R_{TOT}) used for this analysis has a relatively low detection efficiency for neutrons of energy below $\approx$500keV [13], which constitute a large fraction of the pT-neutron spectrum. Hence, there is a significant (possibly up to a factor $\approx$2) systematic error on the resulting $R_{pT}(t)$, which clearly does not affect neither the statistical error on $R_{pT}(t)$ nor the scaling of $R_{pT}(t)$ vs. the fast proton temperature and total energy content reported here. This systematic error (and that coming from possible R_{ADD}) has on the other hand a detrimental impact on a possible diagnostic potential of the pT nuclear reaction (as proposed in [2]), for which an *exact and absolute* measurement of $R_{pT}(t)$ would obviously be needed.

The fast proton distribution function $f_{pFAST,0}(E)$, perpendicular temperature $T_{\perp pFAST,0}$ and density $n_{pFAST,0}$ were measured in the plasma core over the energy range $0.28 \leq E(MeV) \leq 1.1$ using a high-energy Neutral Particle Analyser (NPA) [20, 21]. The NPA is of the E||B type, and views the plasma vertically with its line-of-sight intersecting the plasma midplane at R_{NPA}=3.07m, very close to the magnetic axis, $R_{MAG} \approx$3m. The line-of-sight geometry determines that only ions with $\upsilon_\perp/\upsilon_\| \geq 200$ can be detected by the NPA, where $\upsilon_\perp$ and $\upsilon_\|$ are the ions' velocities perpendicular and parallel to the toroidal magnetic field, respectively. Hence the JET high-energy NPA measures the distribution function of ICRF-driven protons at the tip of their banana orbit in the plasma core. There are eight energy channels in the range $0.2 \leq E(MeV) \leq 3.5$, with common charge and mass selection, thus only one ion species can be measured at any one time. The MeV-energy protons escape the plasma after having been neutralised in the plasma core via electron recombination and charge-exchange reactions with background impurity ions and thermal and high-energy neutral atoms, such as those provided by NBI heating. A detailed description of the techniques used to infer $f_{pFAST,0}(E)$, $T_{\perp pFAST,0}$ and $n_{pFAST,0}$ from the measured atomic flux is given in Refs.[22-26].

Two different ICRF heating schemes were used in the experiments reported here: single-frequency (monochromatic) and multi-frequency (polychromatic). For monochromatic heating, the location of the peak (R_{ABS}) in the ICRF power deposition profile is on the magnetic axis (R_{MAG}). For the case of a strong first pass absorption, the RF power deposition profile can be very well approximated with a Gaussian shape with half-width at half-maximum (w_{ABS}) of the order of the Doppler shift of the resonance [24-28], $w_{ABS} \approx v_{th\|p}/\Omega_p$, hence giving $R_{ABS}=R_{MAG}$ and $w_{ABS} \approx$20cm. Here $v_{th\|p} \approx (2T_{\|pFAST}/m_p)^{1/2}$

is the parallel thermal velocity of the MeV-energy protons, with $T_{\parallel pFAST} \approx T_{\perp pFAST}/10$, Ω_p is the 1st harmonic cyclotron angular frequency for the protons. Using a similar argument for polychromatic heating, the total power deposition profile is given by the convolution of those obtained at each individual ICRF antenna frequency. The width of the power deposition profile can then be empirically approximated by the geometric mean of the sum of the Doppler width w_{ABS} and the position of each R_{ABS} weighted over the relative power density absorbed at the various location [28], giving the value $w_{ABS} \approx 35$cm for the cases considered here. Hence, for the same proton density and ICRF power, the polychromatic heating scheme gives rise, in general, to a lower $T_{\perp pFAST}$ in the plasma core [28-30]. This can be understood by considering the Stix's scaling $T_{\perp FAST} \propto \rho_{ABS}/n_{FAST}$ [27], where ρ_{ABS} is the absorbed ICRF power density.

As typical examples of our measurements, we consider #61259 for the polychromatic heating case, and #61257 for the monochromatic heating case, respectively. Figure 2a shows the main plasma and ICRF heating parameters, and fig2b shows the measured and fitted $\log_{10}(f_{pFAST,0}(E))$ at various time points of interest for #61259. Figures 3a and 3b show the same data for #61257. The NPA measurements were performed with a 4ms time resolution: the raw data were then integrated over 20-50ms, depending on the ion count rate, to obtain $f_{pFAST,0}(E)$ with a statistical error below <50%, hence a maximum error on the inferred $T_{\perp pFAST,0}$ not exceeding $\approx 15\%$ [23]. By integrating $f_{pFAST,0}(E)$ over the energy range of the measurements, one then obtains $n_{pFAST,0}$. We have also verified the value of $n_{pFAST,0}$ using the magnetic measurement of the total fast ion energy content:

$$W_{pFAST} = \int dV n_{pFAST}(r) \left[T_{\perp pFAST}(r) + \frac{1}{2} T_{\parallel pFAST}(r) \right] \approx 4.2\pi^2 a^2 R_{MAG} \int_0^1 dx x \kappa(x) n_{pFAST}(x) T_{\perp pFAST}(x) . \qquad [1]$$

Here x=r/a is the normalised minor radius, r being the radial coordinate along the plasma midplane, a is the plasma minor radius, and we have considered for simplicity that $T_{\parallel pFAST} \approx T_{\perp pFAST}/10$ [11, 24-26]. Cylindrical geometry (without Shafranov shift) has been used to perform the volume integration: the JET toroidal geometry has been taken into account in a simplified form by considering only the elongation $\kappa(x)$ of the magnetic flux surfaces. It should be noted that this analytical result reproduces within the error bar of the magnetic measurements the full calculation of W_{pFAST} considering the exact toroidal geometry [24-26]. To evaluate Eq.(1) we have used the $T_{\perp pFAST,0}$ and $n_{pFAST,0}$ as measured by the high energy NPA in the plasma core. For the fast proton perpendicular tail temperature we have used the Gaussian profile $T_{\perp pFAST}(x)=T_{\perp pFAST,0}*\exp[-(x-x_{ABS})^2/w^2_{ABS}]$, with $x_{ABS}=(R_{ABS}-R_{MAG})/a$ and w_{ABS} given by ICRF power deposition [25, 26, 28]. For the fast proton density we have considered a

parabolic profile: $n_{pFAST}(x)=n_{pFAST,0}*[0.05+0.95*(1-x^2)]$ [23, 24]. With this approach, and considering that the error on the magnetic measurement of W_{pFAST} is of the order of 20%, we estimate the error on n_{pFAST} to be of the order of 30%. For the polychromatic heating case (#61259) we have that $T_{\perp pFAST,0}\approx430keV$ during the steady-state ICRF heating phase (P_{RF}=5.5MW, with a volume-average proton density $\langle n_{pFAST}\rangle\approx1.4\times10^{17}m^{-3}$), compared to $T_{\perp pFAST,0}\approx490keV$ for #61257, the monochromatic heating case with higher P_{RF}=7.5MW and $\langle n_{pFAST}\rangle\approx5\times10^{17}m^{-3}$. This is clearly consistent with the expected lower $T_{\perp pFAST,0}$ for polychromatic heating for the same P_{RF} and $\langle n_{pFAST}\rangle$.

Figures 4a and 4b show the measurements of the pT neutron rate for #61259 and #61257, respectively. In both these discharges approximately 3mg of tritium were puffed at the beginning of the ICRF heating phase, with some additional tritium from previous discharges due to recycling from the walls. We notice that the short 200ms blip of diagnostic NBI around t=48.5sec causes an approximately three-fold increase in R_{TOT}, due to the DT reactions.

Table 1 gives an overview of the ICRF heating and high energy proton parameters for all the seven discharges analysed in this work. In order to determine a scaling of R_{pT}=f($T_{\perp pFAST0}$, W_{pFAST}) we have focused our attention to time-windows with ICRF-only heating, i.e., removing the time window where the diagnostic NBI blip was applied, including 300ms at the end of the blip to allow for the slowing-down of the NBI ions.

Shot	R_{pT}(neut/s)	Tpuff	n_T/n_e	ICRF heating	$T_{\perp pFAST}$	$\langle n_{pFAST}\rangle$	W_{pFAST}
61254	9.70×10^{13}	*no puff*	0.18%	6.6÷7.2MW, mono	450keV	$5.7\times10^{17}m^{-3}$	0.61MJ
61256	1.21×10^{14}	*no puff*	0.15%	6.3÷7.2MW, mono	446keV	$5.9\times10^{17}m^{-3}$	0.73MJ
61257	2.95×10^{14}	3.0mg	0.35%	7.1÷7.4MW, mono	486keV	$4.8\times10^{17}m^{-3}$	0.68MJ
61258	3.14×10^{14}	5.1mg	0.42%	7.4÷7.6MW, mono	461keV	$5.4\times10^{17}m^{-3}$	0.69MJ
61259	1.35×10^{14}	3.2mg	0.50%	4.6÷5.6MW, poly	430keV	$1.4\times10^{17}m^{-3}$	0.59MJ
61260	8.77×10^{13}	3.0mg	0.63%	4.3÷6.3MW, poly	450keV	$2.2\times10^{17}m^{-3}$	0.55MJ
61261	6.15×10^{13}	5.1mg	0.89%	2.7÷4.5MW, mono	287keV	$6.5\times10^{17}m^{-3}$	0.31MJ
Table 1. *Main plasma parameters for the set of discharges considered in this work.*							

For the purpose of illustration, the data presented in Table 1 were averaged over the entire steady-state ICRF heating phase. Here W_{pFAST} is the magnetic measurement of the fast proton total energy content, $W_{FAST}=W_{DFAST}+W_{pFAST}$, $W_{FAST}=4(W_{DIA}-W_{PLASMA})/3$-*offset*, where W_{DIA} is the diamagnetic energy and W_{PLASMA} is the plasma stored energy and W_{DFAST} is NBI fast ion energy (see the discussion in Ref.[31], Eq.(10), which unfortunately has the wrong numerical coefficient due to a typo: note that by

eliminating the NBI time window, no contribution to W_{FAST} from the NBI high energy deuterons is expected, hence $W_{FAST}=W_{pFAST}$). Note also that we have set $R_{pT}=0$ over the NBI heating phase by default.

We notice from the comparison between fig4a and fig4b that the effect of the different heating scheme is mainly to change the fast proton temperature and energy content for a given P_{RF} and $<n_{pFAST}>$. Hence, it is possible to combine the data from these two different experimental scenarios into one single database and compare the value of R_{pT} simply as function of the fast ion temperature and energy content. Moreover, an exact analytical model of the dependence of R_{pT} on the measured $T_{\perp pFAST,0}$ and W_{pFAST} can be obtained by considering that the JET high-energy NPA measures the distribution function of ICRF-driven protons at the tip of their banana orbit in the plasma centre.

Although the precision of this model calculation is somewhat hampered by the limited knowledge of the actual distribution function of the fast protons, this analysis provides however a clear demonstration that the inferred absolute values of R_{pT} are indeed reasonable and in sufficiently good agreement with the direct R_{pT} measurements, which in turns considerably strengthens our overall conclusions about the dependence of R_{pT} on the fast proton temperature and total energy content. This analytical calculation also provides upper bounds for the errors associated with our models for the fast proton distribution function, as it will be shown in fig5a by comparing the different estimates obtained for R_{pT} by using different models for the fast proton distribution functions.

The model analytical calculation of $R_{pT}(T)$ starts by using phase-space conservation for the fast proton distribution function, i.e. $f(\underline{\upsilon};x)d\underline{\upsilon}=F(E;x)dE$, so that we can formulate $R_{pT}(T)$ as:

$$
\begin{aligned}
&R_{pT}(T) = \int dV n_{pFAST}(x) n_T(x) \int d\overline{\upsilon} f_{pFAST}(\overline{\upsilon},x) \sigma_{pT}(\upsilon) \upsilon \\[2mm]
&R_{pT}(T) = 8\pi^3 a^2 R_{MAG} \int_0^1 dx \kappa(x) n_{pFAST}(x) n_T(x) \int_0^\infty d\upsilon_\perp \upsilon_\perp \int_{-\infty}^\infty d\upsilon_\parallel f_{pFAST}(\upsilon_\perp,\upsilon_\parallel;x) \sigma_{pT}\left(\sqrt{\upsilon_\perp^2+\upsilon_\parallel^2}\right)\sqrt{\upsilon_\perp^2+\upsilon_\parallel^2} \\[2mm]
&R_{pT}(T) = 8\pi^3 a^2 R_{MAG} \int_0^1 dx \kappa(x) n_{pFAST}(x) n_T(x) I_{pT}(T,x) \\[2mm]
&I_{pT}(T,x) = \int_0^\infty d\upsilon_\perp \upsilon_\perp \int_{-\infty}^\infty d\upsilon_\parallel f_{pFAST}(\upsilon_\perp,\upsilon_\parallel;x) \sigma_{pT}\left(\sqrt{\upsilon_\perp^2+\upsilon_\parallel^2}\right)\sqrt{\upsilon_\perp^2+\upsilon_\parallel^2} = \frac{1}{2\pi}\int_0^\infty dE \sqrt{E} \sigma_{pT}(E) F_{pFAST}(E,x)
\end{aligned}
\qquad . \quad [2]
$$

Here $\underline{\upsilon}=(\upsilon_\perp^2 e_\perp,\ \upsilon_\parallel e_\parallel,\ \phi e_\phi)$ is the 3D velocity vector, and for simplicity we have assumed toroidal homogeneity of $F_{pFAST}(E;x)dE=2\pi f_{pFAST}(\upsilon_\perp,\upsilon_\parallel;x)\upsilon_\perp d\upsilon_\perp d\upsilon_\parallel$. Following the derivation of Ref.[24], the measured (bi-Maxwellian) fast proton distribution function can therefore be analytically expressed as function of the parallel ($T_\parallel$) and perpendicular ($T_\perp$) tail temperature as:

$$F_{pFAST,1}(E,x) = \frac{2C_1(E,x)}{\sqrt{\pi}(1-\alpha)\left[1-3\alpha^2(1-\alpha)/2\right]} \frac{1}{T_\perp(x)} \sqrt{\frac{E}{T_\parallel(x)}} \exp\left(-\frac{E}{T_{EFF}(x)}\right)\left[1-\frac{\alpha^2 E}{T_\perp(x)}\right] . \quad [3]$$

Here $C_1(E,x)$ is a normalisation constant such that $\int F_{pFAST,1}(E)dE=1$, $\alpha(x)=[T_\perp(x)-T_{EFF}(x)]/T_\perp(x)$ and $T_{EFF}(x)$ is the overall effective temperature of the bi-Maxwellian distribution function $f(\upsilon_\perp,\upsilon_\parallel)$ defined as $T_{EFF}=[T(E_*)/G(E)]\times[dG(E)/dE]_{(E=E_*)}$, where E_* is the median energy of $F(E)$, $G(E)=F(E)/\sqrt{E}$ and $T(E_*)$ is the temperature deduced from the leading order Maxwellian term of Eq.(3). A practical analytical model for $T_{EFF}(x)$ can be derived from the analysis presented in Refs.[24-26] as:

$$T_{EFF}(x) = \frac{\sqrt{\pi}}{2\sqrt{5}} \sqrt{\frac{4T_\perp^2(x)+T_\parallel^2(x)}{1-T_\parallel(x)/T_\perp(x)}} erf\left(\sqrt{1-\frac{T_\parallel(x)}{T_\perp(x)}}\right) \xrightarrow[T_\parallel(x)<<T_\perp(x)]{} \sqrt{\frac{4}{5}}T_\perp(x) . \quad [4]$$

Note that this derivation would conserve the isotropy of the distribution function in the cases where $T_\parallel=T_\perp=T$, since it then gives $T_{EFF}=T$. Note however that these specific cases are not those dealt with in this work, as for ICRF heating we do have indeed a strong anisotropy, $T_\parallel<<T_\perp$, hence $T_{EFF}\approx T_\perp$. Alternatively, following the derivation of Refs.[25, 26], a model pitch-angle-averaged distribution function for the high-energy protons can be obtained for $T_\parallel\neq T_\perp$ as:

$$F_{pFAST,2}(E,x) = \frac{C_2(E,x)}{T_{EFF}(x)\sqrt{1-T_\parallel(x)/T_\perp(x)}} \exp\left(-\frac{E}{T_{EFF}(x)}\right) erf\left(\sqrt{\frac{E}{T_\parallel(x)}}\sqrt{1-\frac{T_\parallel(x)}{T_\perp(x)}}\right), \quad [5]$$

where $C_2(E,x)$ is, again, a normalisation constant such that $\int F_{pFAST,2}(E)dE=1$, and we used the definition of the error function $erf(z)$.

The averaging of $<\sigma_{pT}(\upsilon)\upsilon>$ over $F_{pFAST}(E;x)$ or $f_{pFAST}(\underline{\upsilon},x)$, i.e. the integral $I_{pT}(T,x)$ entering Eq.(2), can be performed numerically using the two analytic model distribution functions of Eq.(3) and Eq.(5), which are rather different from the single-Maxwellian model $f_{pFAST}(E)=C_0\exp(-E/T)/T$ of Refs.[2, 32]. In particular, we note that the energy (or velocity) and space integration required to compute $R_{pT}(T)$ are now heavily convoluted due to the dependence of $T_\perp=T_\perp(x)$. This analytic treatment for $I_{pT}(T,x)$ can be taken further by considering the local normalised energy $t=E/T_{EFF}(x)=(E/T_0)*\exp(z(x)^2)/(1-\alpha(x))=t(x)$, where $z=(x-x_0)/\Delta$, and expanding $\exp[-\exp(z^2)]=\exp(-\Sigma_n z^n/n!)$. The full series expansion leads to the exact but rather cumbersome expression $I_{pT}(x,T_0)=\Sigma_n C_n z(x)^n K_{(2n+1)/4}(z(x),T_0)/(1-\alpha(x))^n$, where the functions K's are modified Bessel functions of rational order. This series expansion is primarily useful to separate the x and T_0 variables in the energy integral giving $I_{pT}(T,x)$. Considering now only a 2nd

order z-expansion, redefining the variable t=E/T_{EFF}(x=0), using $\alpha_0=\alpha$(x=0) and $\beta(x)=T_{\parallel}(x)/T_{\perp}(x)$, with $\beta_0=\beta$(x=0), we finally obtain for $I_{pT}(T_0,x)$ the much more manageable expressions:

$$I_{pT,1}(x,T_0) = \frac{2\sqrt{1-\alpha(x)}}{\sqrt{\pi}\left[1-3\alpha(x)^2\left(1-\alpha(x)\right)/2\right]}\sqrt{T_0}\exp\left(-\frac{z(x)^2}{2}\right)\int\limits_0^\infty dt\sigma(t)C_1(t,x)te^{-t}\left[1-\alpha_0^2\left(1-\alpha_0\right)t\right],$$ [6a]

$$I_{pT,2}(x,T_0) = \frac{\sqrt{1-\alpha(x)}}{\sqrt{1-T_{\parallel}(x)/T_{\perp}(x)}}\sqrt{T_0}\exp\left(-\frac{z(x)^2}{2}\right)\int\limits_0^\infty dtC_2(t,x)\sigma(t)\sqrt{t}e^{-t}erf\left(\sqrt{t}\sqrt{\frac{T_{EFF}(x)}{T_{\parallel}(x)}}\sqrt{1-\frac{T_{\parallel}(x)}{T_{\perp}(x)}}\right)$$

$$I_{pT,2}(x,T_0) = \frac{\sqrt{1-\alpha(x)}}{\sqrt{\left(1-\beta(x)\right)/\beta(x)}}\sqrt{T_0}\exp\left(-\frac{z(x)^2}{2}\right)\int\limits_0^\infty dtC_2(t,x)\sigma(t)\sqrt{t}e^{-t}erf\left(\sqrt{t}\sqrt{1-\alpha_0}\sqrt{\frac{1-\beta_0}{\beta_0}}\right)$$ [6b]

To perform this analytical computation of R_{pT}, we consider Gaussian-type radial profiles for the fast proton perpendicular and parallel temperatures, as given by ICRF physics: $T_{\perp}(x)=T_0*\exp[-(x-x_0)^2/\Delta^2]$ and $T_{\parallel}(x)=T_e(x)+0.1*[T_{\perp}(x)]^{0.8}$. We also assume the following model parabolic radial profiles for the fast proton and thermal triton density, the electron temperature and the plasma elongation:

$n_p(x) = n_{p0}\left[a_1 + \left(1-a_1\right)\left(1-x^2\right)^{\gamma_1}\right],$	$a_1=0.05, \gamma_1=1;$	[7a]
$n_T(x) = n_{T0}\left[a_2 + \left(1-a_2\right)\left(1-x^2\right)^{\gamma_2}\right],$	$a_2=0.1, \gamma_2=1;$	[7b]
$T_e(x) = T_{e0}\left[a_3 + \left(1-a_3\right)\left(1-x^2\right)^{\gamma_3}\right],$	$a_3=0.1, \gamma_3=1.5;$	[7c]
$\kappa(x) = \kappa_0 + \kappa_1 x^2 + \kappa_2 x^4,$	$\kappa_0=1.2, \kappa_1=0.25, \kappa_2=0.2.$	[7d]

For illustration purposes, we have taken $x_0=0.05$, $\Delta=0.2$ to determine the profile of $T_{\perp}(x)$, i.e., here we consider explicitly only the case of monochromatic heating.

Figure 5a presents the scaling of the measured R_{pT} as function of $T_{\perp pFAST,0}$ and W_{pFAST} for the data points obtained during the ICRF-only heating phase of the discharges indicated in Table 1, together with the calculated values using different approximations for the distribution function of the high-energy protons. We have focused our attention primarily to the data points collected over the steady-state heating phase, where we typically have that $T_{\perp pFAST,0}$(keV)=250÷550. In addition to these points, which constitute the bulk of our data, we have also considered data points collected during the transient phases (ICRF power switch on/off) to provide boundary values for the R_{pT} scaling at low $T_{\perp pFAST,0}$ and W_{pFAST}. In fig5a we have normalised the measured and computed R_{pT} with respect to the tritium concentration n_T/n_e and the fast proton concentration <n_{pFAST}/n_e> (as given in Table 1) to take into account the changing (p, T) ion densities over the various discharges considered in this work. This

removes from our database the obvious density dependency $R_{pT} \propto n_T n_{pFAST}$. We have then integrated the time-resolved measurements of $R_{pT}(t)$ over a sufficiently long time window (typically 50-100ms) to reduce the maximum statistical error on $R_{pT}(t)$ to no more than 30%. Finally, to remove some cluttering from fig5a, we have reduced the number of points by clustering the individual $R_{pT}=f(T_{\perp pFAST,0}, W_{pFAST})$ data points over a smaller number of close-by values of $T_{\perp pFAST,0}$ and W_{pFAST}, since values of $R_{pT} \pm \sigma_{RPT}$ are obtained for values of $T_{\perp pFAST,0}$ and W_{pFAST} within their respective statistical error. Note that this approach conserves the database marginals, i.e. the global probability function in the "reduced" database for the measured R_{pT} to be in a certain range of $T_{\perp pFAST,0}$ and W_{pFAST} does not change by more than $\sigma_{RPT}/2$ in the original database. Therefore, the error bars shown in fig5a are the sum of the uncertainties in the measurements together with the scatter in the "original" data, which was implicitly smoothed out through this clustering process.

The variations between the calculated R_{pT} are related to the differences in the radial profiles of the fast proton distribution functions used for this calculations. The qualitative and quantitative agreement between the measured and computed values of R_{pT} is strikingly remarkable considering the very simple analytical models we have used for the fast proton distribution function, the plasma geometry and the background plasma parameters. This further confirms that the detailed kinematics of the pT-neutron production does not affect this scaling, as we are not considering the *precise details* of the neutron energy spectra (for instance: the number of pT-neutrons per unit solid angle in different energy ranges), but only the *total number* of measured pT-neutrons (i.e., the value integrated over the full energy range of the measurements made with the JET neutron detectors). Moreover, this agreement gives rise to some optimism towards possible future uses of the pT-fusion reactions for diagnostic purposes, as proposed in [2], provided an exact absolute calibration of the measured R_{pT} data can be routinely achieved.

Figure 5a shows that R_{pT} increases almost linearly with $T_{\perp pFAST,0}$ for $T_{\perp pFAST,0}>200keV$, being very small and almost constant for $T_{\perp pFAST,0}<200keV$, consistent with the much lower number of protons with high energy $E_{pCM}>764keV$ for lower $T_{\perp pFAST,0}$. The almost linear dependence $R_{pT} \propto T_{\perp pFAST,0}$ is not a trivial result: $R_{pT} \propto n_T n_{pFAST} \times <\sigma_{pT}(v)\upsilon_{pFAST}>$, averaged over the fast proton distribution function and integrated over the plasma volume. Similarly, R_{pT} increases almost linearly with W_{pFAST} up to $W_{pFAST} \approx 700kJ$, and then shows some indication of possible saturation at higher W_{pFAST}, where many R_{PT} points are bunched together for $W_{pFAST}(kJ)=700 \rightarrow 810$. This is particularly clear when comparing the measurements with the calculated values. However, since the range of the W_{pFAST} measurements for the discharges considered here does not exceed $W_{pFAST} \approx 810kJ$, it is not possible to substantiate this

11

experimental result more systematically. The saturation of R_{pT} at high W_{pFAST} could be due to radial diffusion of the high energy protons induced by the magneto-hydrodynamic instabilities observed in the discharges considered here, such as Alfvén Eigenmodes and fishbones.

Considering now the role of additional neutron producing mechanisms, summed up in the general R_{ADD} term described earlier, we note that, when neglecting recycling from the walls, the first two discharges in our database should have $R_{pT}=0$ as there was no tritium gas puff. Hence, as a pessimistic estimate for such R_{ADD}, we can consider that all *supposed* pT neutrons for these two discharges must actually be accounted for by R_{ADD}, hence subtract this value from the other discharges as a background, and repeat the procedure used to obtain fig5a which was described above. Figure 5b then shows the result of this further analysis: we note that the approximately linear scaling of $R_{pT}=f(T_{\perp pFAST,0}, W_{pFAST})$ determined from fig5a is maintained but now with a different offset. This confirms that even in the worst case, the various R_{ADD} mechanisms are only introducing a systematic error in the analysis reported here.

In summary, the dependence of the pT neutron rate R_{pT} has been analysed as a function of the core perpendicular fast proton temperature $T_{\perp pFAST,0}$ and proton energy content W_{pFAST} for monochromatic and polychromatic ICRF heating. It is found that R_{pT} increases almost linearly with $T_{\perp pFAST,0}$ in the range $200<T_{\perp pFAST,0}(keV)<600$. This scaling is non-trivial, as we have demonstrated using two distinct analytic formulations for the fast proton distribution function. No appreciable difference can be related to the different ICRF heating scheme, their main effect being that of producing a different $T_{\perp pFAST}(x)$. Similarly, R_{pT} increases almost linearly with W_{pFAST}. At the largest values of $W_{pFAST}>700kJ$, the error bars prevent us from drawing strong conclusions regarding a possible saturation of R_{pT} at these values of W_{pFAST} which could be expected if the fast protons were to be depleted from the plasma core at higher fast proton temperature due to radial transport induced by magneto-hydrodynamic instabilities.

References.

1. H.Liskien and A.Paulsen, Nucl. Data Tables **11** (1973), 569.

2. M.Santala et al., Plasma Phys. Control. Fusion **48** (2006), 1233.

3. J.Wesson, *Tokamaks*, 3rd edition, (Oxford Science Publication, Oxford, 2003), p.617.

4. G.Kaye and T.Laby, *Tables of Physical and Chemical Constants*, Longman Publishing, London (1995), page 546 and following.

5. Progress in the ITER Physics Basis, Nucl. Fusion **47** (2007).

6. H.Henriksson et al., Plasma Phys. Control. Fusion **44** (2002), 1253.

7. M.Tardocchi et al., Nucl. Fus. **42** (2002), 1273.

8. H.Henriksson et al., Plasma Phys. Control. Fusion **47** (2005), 1763.

9. M.Mantsinen et al., Nucl. Fusion **41** (2001), 1815.

10. K.-D.Zastrow et al., Plasma Phys. Control. Fusion **46** (2004), B255.

11. D.Stork et al., Nucl. Fusion **45** (2005), S181.

12. L.Bertalot et al., Fusion Engineering and Design **74** (2005), 835.

13. M.Swinhoe and O.Jarvis, Nucl. Instrum. Meth. **221** (1984), 460.

14. M.Loughlin et al., Rev. Sci. Instrum. **70** (1999), 1123.

15. B.Esposito et al., Rev. Sci. Instrum. **75** (2004), 3350.

16. S.Popovichev et al., *Performance of neutron measurements during JET trace tritium experiments*, Proceedings 31st EPS Conference on Controlled Fusion and Plasma Physics, London (UK), 2004, see http://epsppd.epfl.ch/London/pdf/P5_173.pdf.

17. Y.Kaschuck et al., *Neutron measurements during trace tritium experiments at JET using a stilbene detector*, Proceedings 31st EPS Conference on Controlled Fusion and Plasma Physics, London (UK), 2004, see http://epsppd.epfl.ch/London/pdf/P5_174.pdf.

18. G.Cenacchi, A.Taroni, *JETTO: a free-boundary plasma transport code*, Report ENEA-RT-T113-88-5, 1988.

19. R.Budny et al., Phys. of Plasmas **7** (2000), 5038.

20. A.Korotkov and A.Gondhalekar, 21st European Physical Society Conference on Controlled Fusion and Plasma Physics, Europhysics Conference Abstract 18-B(1994), I-266.

21. K.McClements et al., Nucl. Fusion **37** (1997), 473.

22. A.Korotkov et al., Nucl. Fusion **37** (1997), 35.

23. C.Schlatter et al., Rev. Sci. Instrum. **75** (2004), 3547.

24. D.Testa, A.Gondhalekar, Nucl. Fusion **40** (2000), 975.

25. D.Testa et al., Phys. Plasmas **6** (1999), 3489.

26. D.Testa et al., Phys. Plasmas **6** (1999), 3498.

27. T.Stix, *Waves in Plasmas*, (American Institute of Physics, New York, USA, 1992), chapter 17.

28. D.Testa et al., Plasma Phys. Control. Fusion **46** (2004), S59.

29. D.Testa et al., Nucl. Fusion **45** (2005), 907.

30. M.Mantsinen et al., *Comparison of monochromatic and polychromatic heating in JET*, Proceedings 15th Topical Conference on Radio Frequency Power in Plasmas, Moran (USA) , edited by Cary B. Forest, Springer-Verlag publication, Plasma Physics Series, vol.694, 2003.

31. L.-G.Eriksson et al., Nucl. Fus. **33** (1993), 1037.

32. M.Santala et al., *pT fusion by RF-heated protons in JET trace tritium discharges*, Proceedings 31st EPS Conference on Controlled Fusion and Plasma Physics, London (UK), 2004, see http://epsppd.epfl.ch/London/pdf/P5_163.pdf.

Figure Captions.

Figure 1. The cross-section for the fusion reaction involving deuterium, tritium and protons (from Ref.[4]). The pT-fusion cross section is the largest between those typically occurring in fusion plasmas for proton energies (in the centre-of-mass frame of reference) above $E_{pCM} > 2MeV$.

Figure 2a. Main plasma and ICRF heating parameters for #61259, the reference polychromatic heating case. Here RFx indicates the four ICRF generators, τ_{SP0} and $<n_p>$ are the core fast ion slowing down time and volume average proton density, respectively, n_{e0} and T_{e0} are the central electron density and temperature, q is the safety factor, and W_{pFAST} is the magnetic measurement of the fast proton energy.

Figure 2b. The measured (markers) and fitted (line) fast ion distribution for #61259 at various time points of interest during the ICRF time window.

Figure 3a. Main plasma and ICRF heating parameters for #61257, the comparison monochromatic heating case at higher P_{RF} and $<n_{pFAST}>$.

Figure 3b. The measured (markers) and fitted (line) fast ion distribution for #61257 at various time points of interest during the ICRF time window.

Figure 4a. The measured excess pT neutron rate for #61259. We notice the almost three-fold increase in the total neutron rate during the diagnostic NBI blip at t=48.5sec (note that we set $R_{pT}=0$ by default over the NBI heating phase, including 300ms slowing-down time) and the almost two-fold increase in the pT-neutrons after the tritium gas puff. As in fig2a, W_{pFAST} is the magnetic measurement of the fast proton energy content.

Figure 4b. The measured excess pT neutron rate for #61257, the monochromatic heating case. As in fig3a, W_{pFAST} is the magnetic measurement of the fast proton energy content. Note that $R_{pT}=0$ by default during the NBI heating phase, including 300ms ion slowing-down time after the NBI blip.

Figure 5a. Scaling of the measured pT neutron rate as a function of the fast proton temperature in the plasma core and the total fast proton energy content. Also shown are the calculated values using three different models for the distribution function of the high energy protons: the bi-Maxwellian model is given in Eq.(3), and the pitch-angle average model is given in Eq.(5).

Figure 5b. Scaling of the measured pT neutron rate as a function of the fast proton temperature in the plasma core and the total fast proton energy content, subtracting the background R_{ADD}.
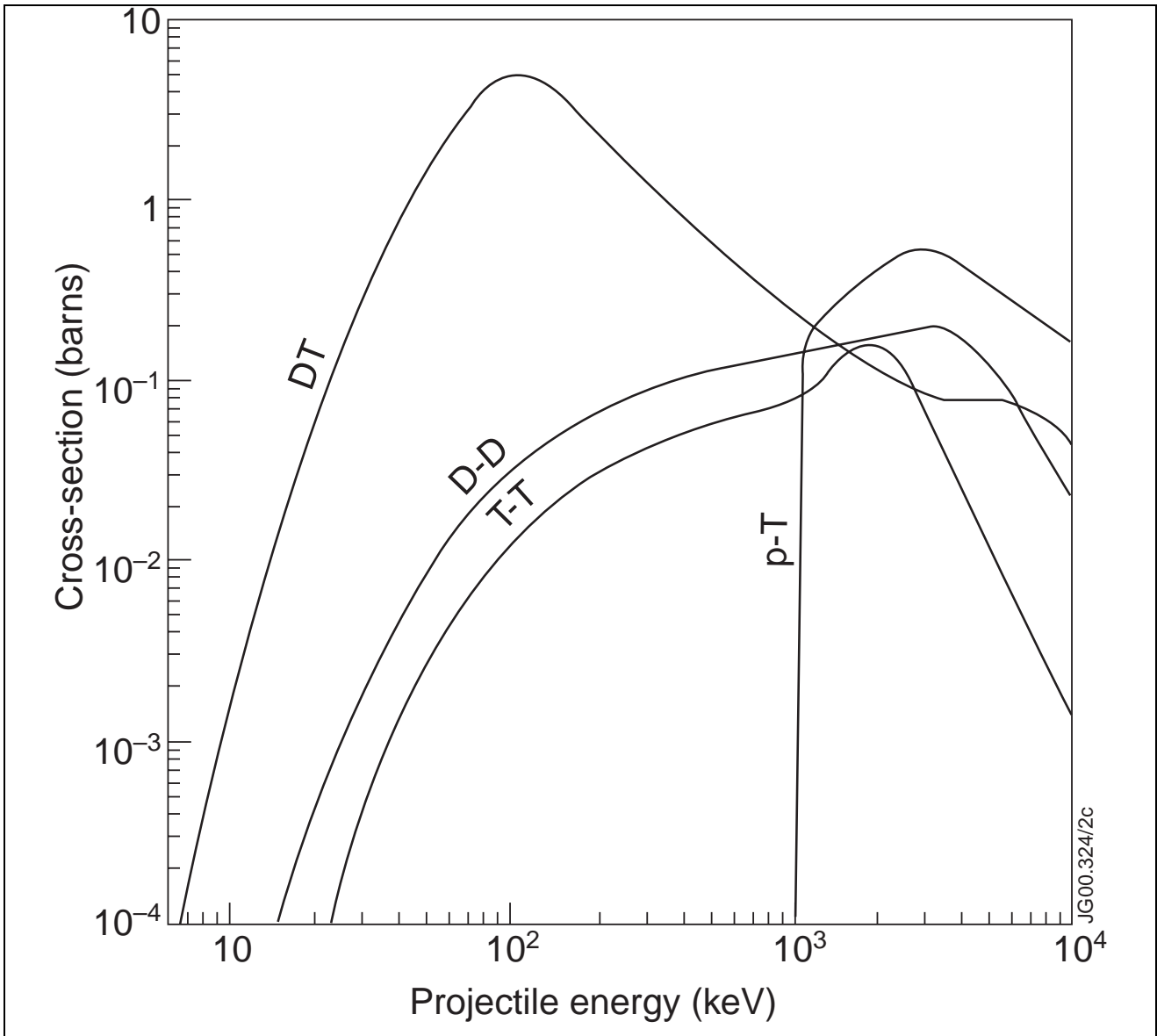
Figure 1. The cross-section for the fusion reaction involving deuterium, tritium and protons (from Ref.[4]). The pT-fusion cross section is the largest between those typically occurring in fusion plasmas for proton energies (in the centre-of-mass frame of reference) above $E_{pCM} > 2$MeV.
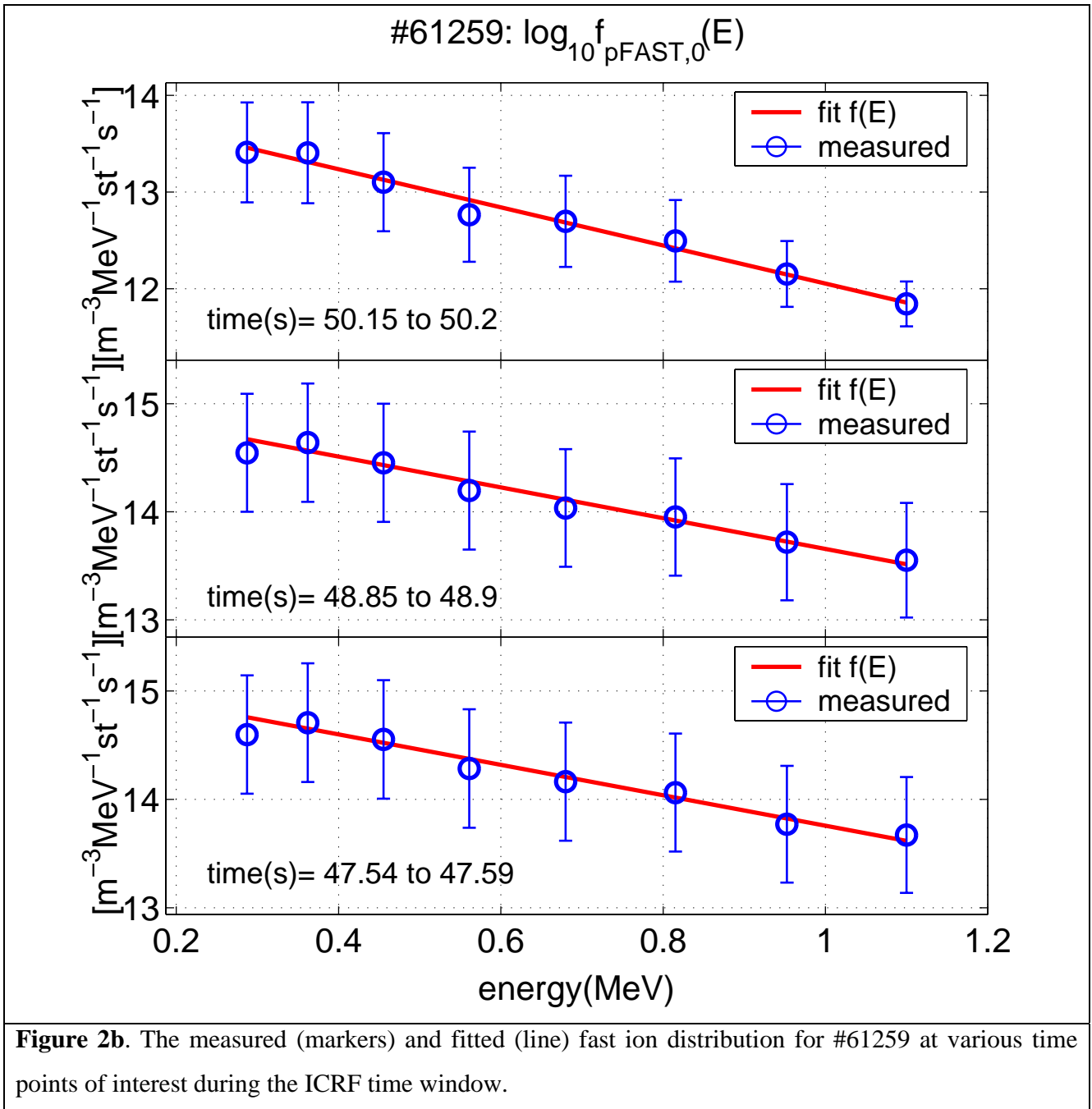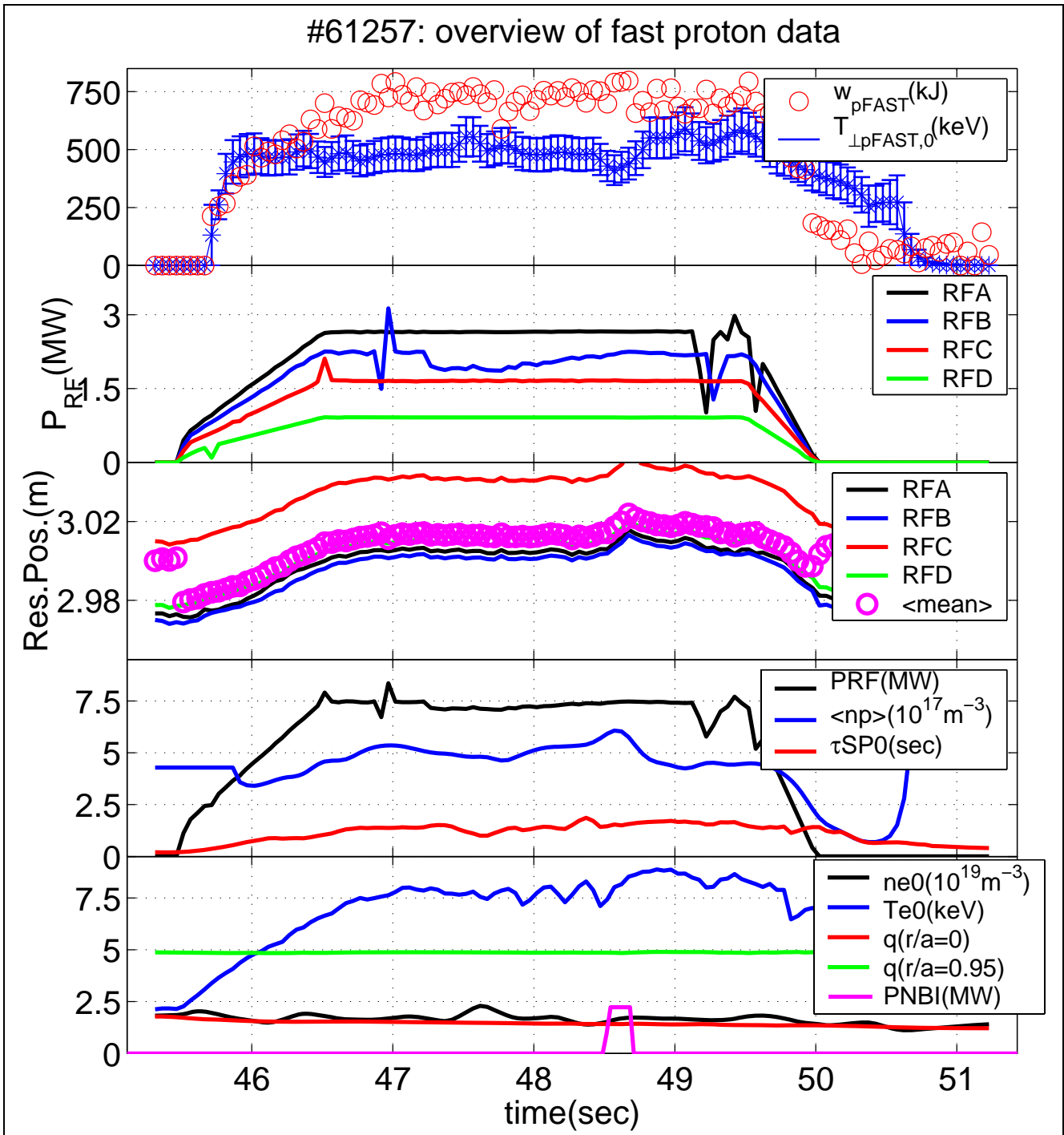
D.Testa et al., Figure 1
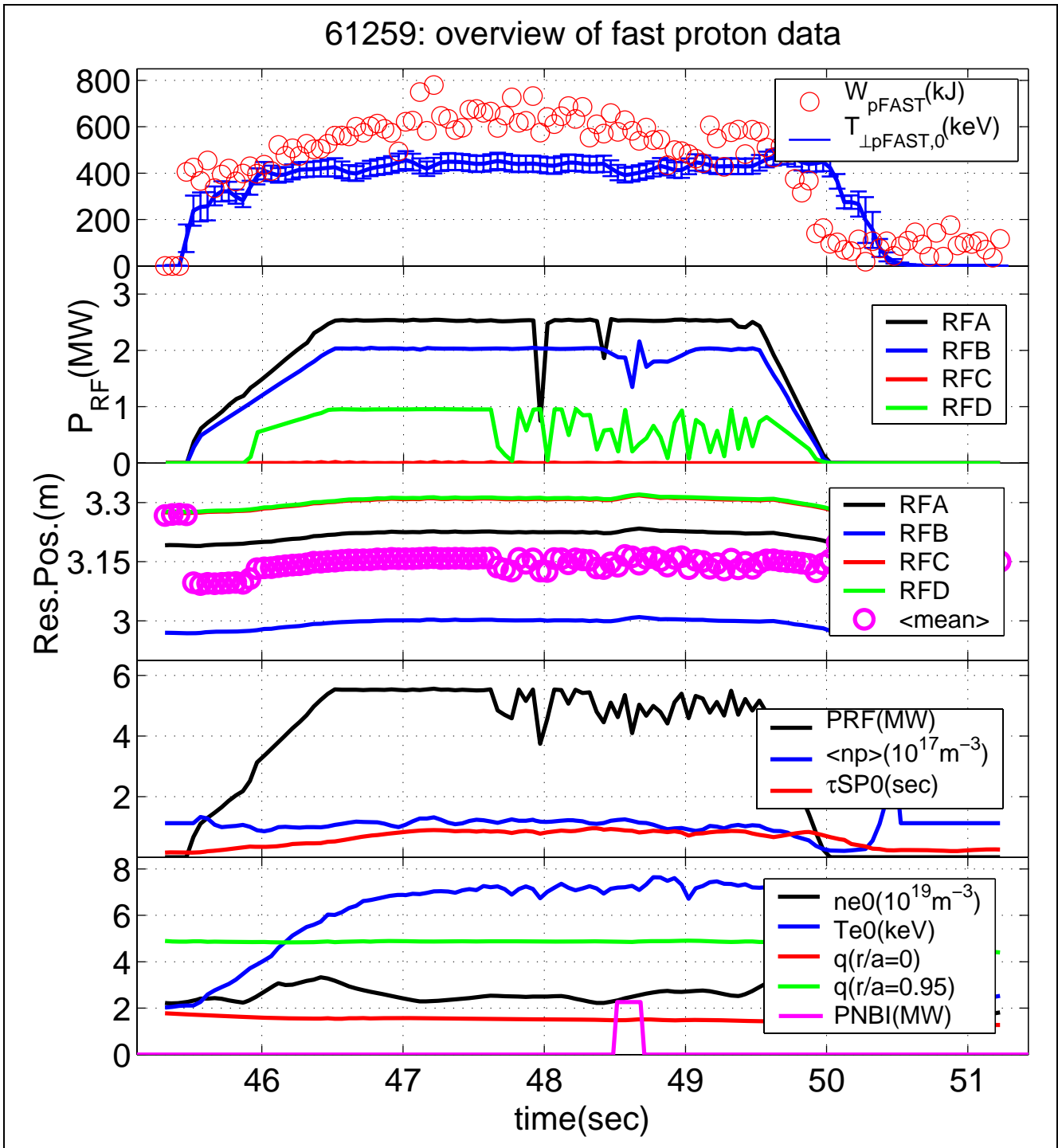
Figure 2a. Main plasma and ICRF heating parameters for #61259, the reference polychromatic heating case. Here RFx indicates the four ICRF generators, τ_{SP0} and $<n_p>$ are the core fast ion slowing down time and volume average proton density, respectively, n_{e0} and T_{e0} are the central electron density and temperature, q is the safety factor, and W_{pFAST} is the magnetic measurement of the fast proton energy.

D.Testa et al., Figure 2a

Figure 2b. The measured (markers) and fitted (line) fast ion distribution for #61259 at various time points of interest during the ICRF time window.
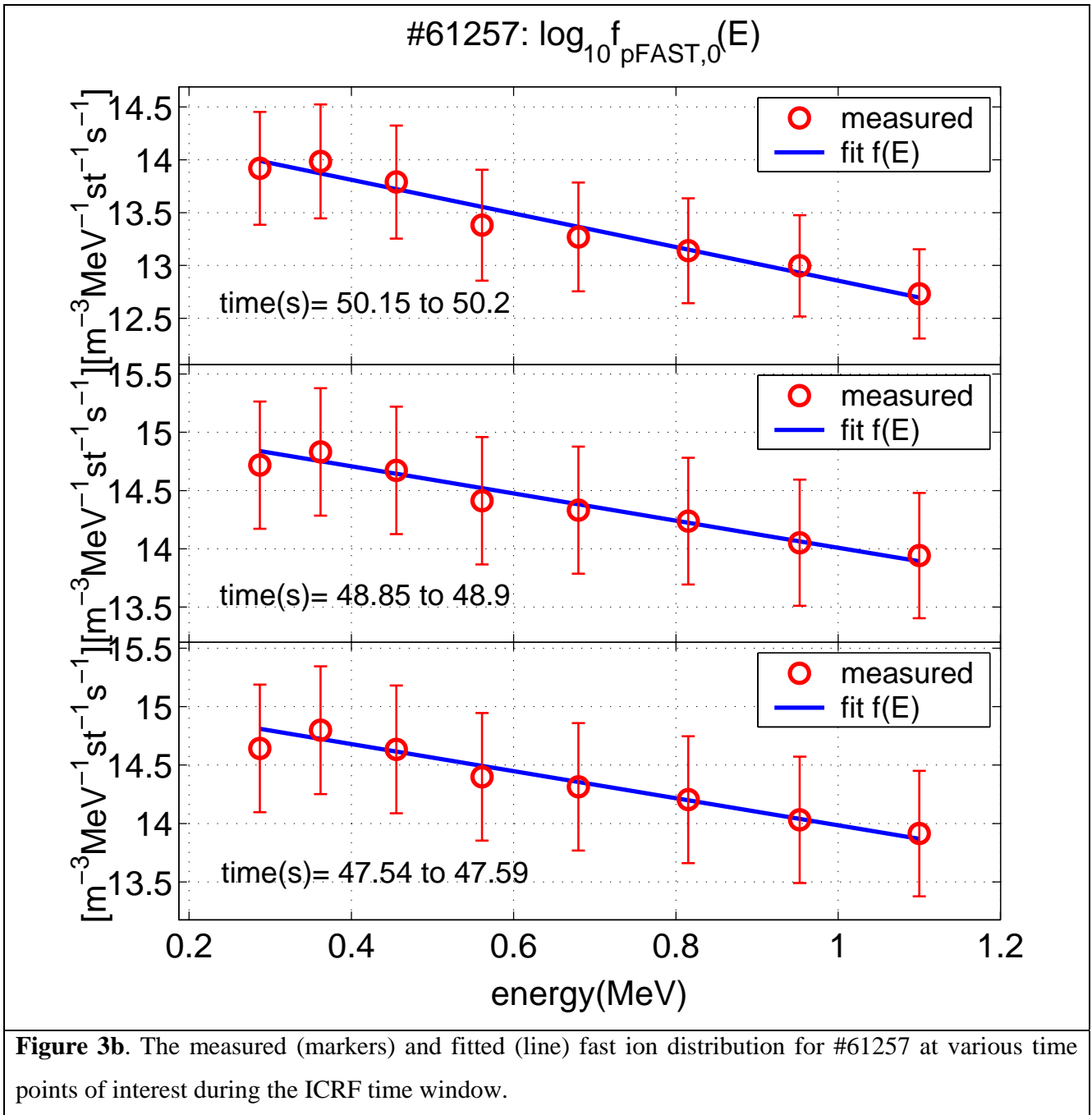
D.Testa et al., Figure 2b
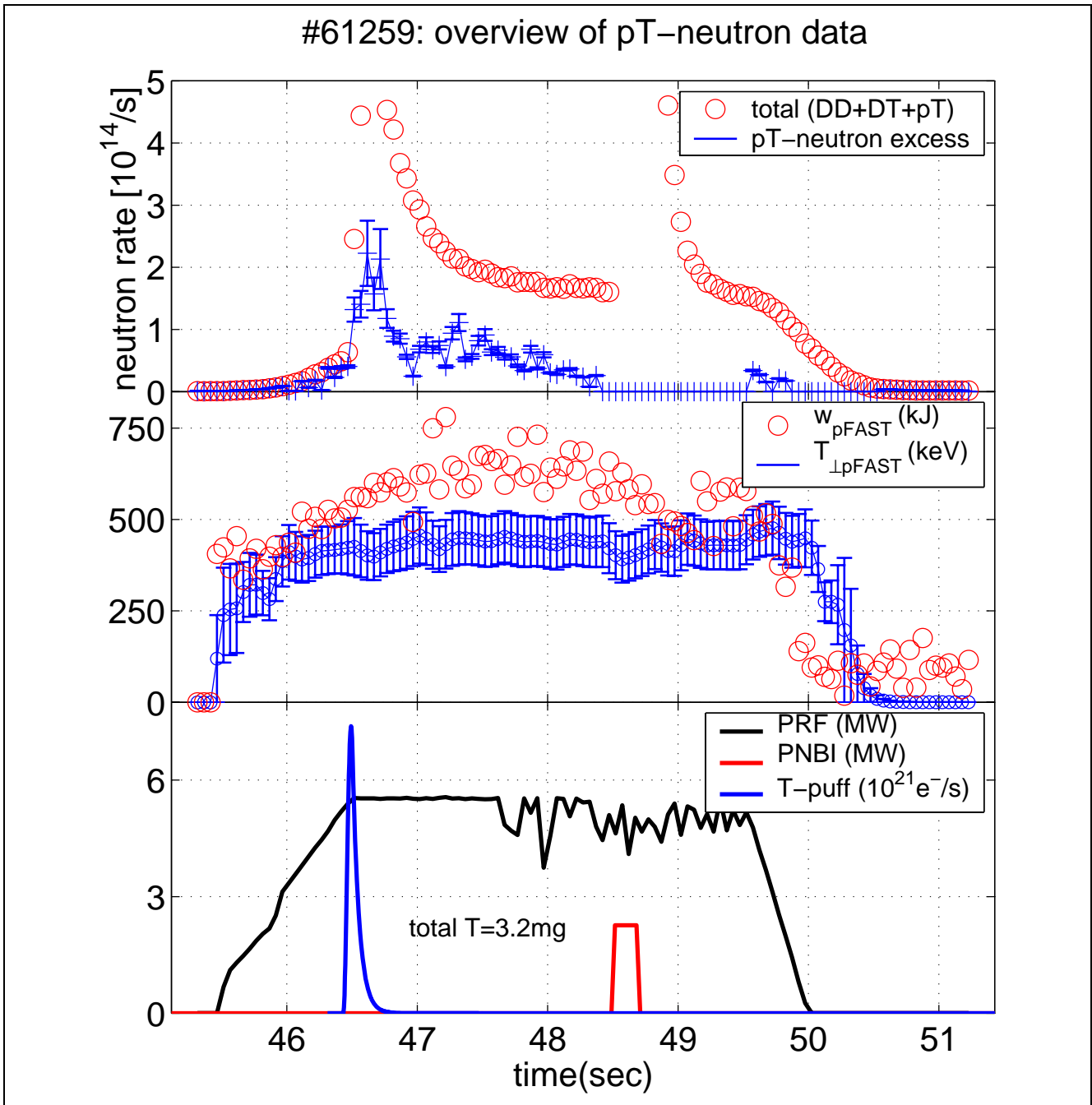
Figure 3a. Main plasma and ICRF heating parameters for #61257, the comparison monochromatic heating case at higher P_{RF} and $<n_p>$.

Figure 3b. The measured (markers) and fitted (line) fast ion distribution for #61257 at various time points of interest during the ICRF time window.

D.Testa et al., Figure 3b

Figure 4a. The measured excess pT neutron rate for #61259. We notice the almost three-fold increase in the total neutron rate during the diagnostic NBI blip at t=48.5sec (note that we set $R_{pT}=0$ by default over the NBI heating phase, including 300ms slowing-down time) and the almost two-fold increase in the pT-neutrons after the tritium gas puff. As in fig2a, W_{pFAST} is the magnetic measurement of the fast proton energy content.
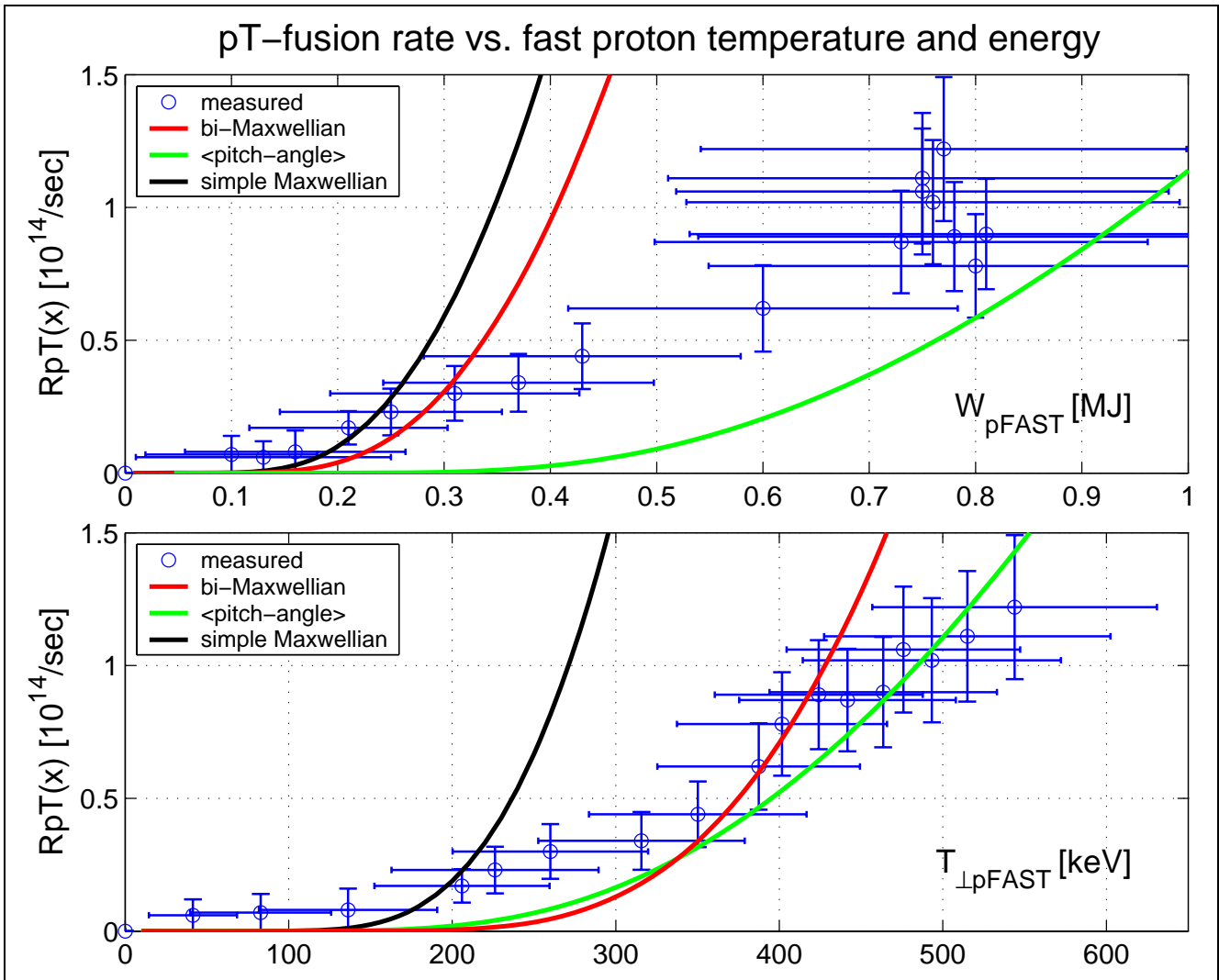
D.Testa et al., Figure 2a
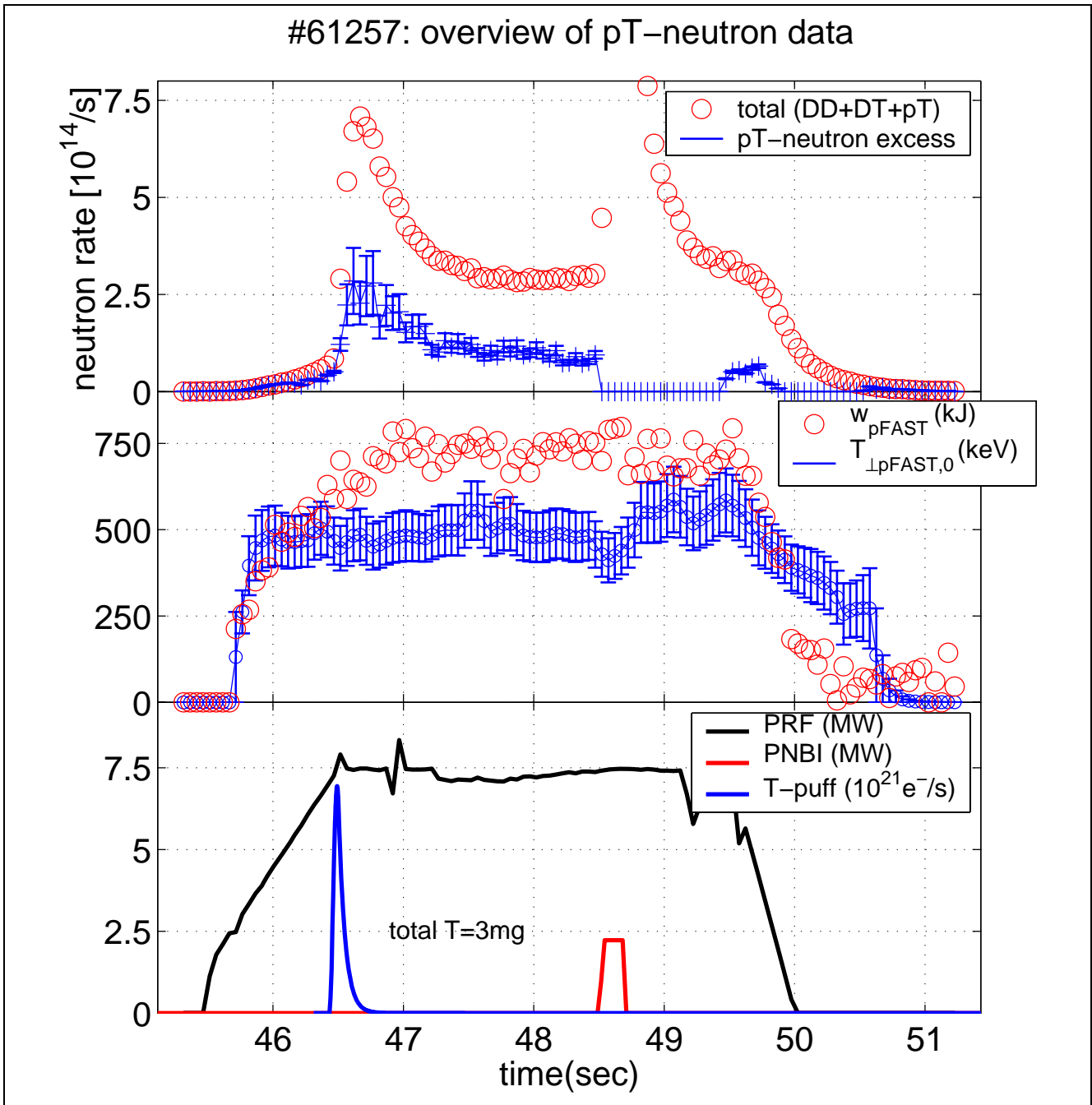
Figure 4b. The measured excess pT neutron rate for #61257, the monochromatic heating case. As in fig3a, W_{pFAST} is the magnetic measurement of the fast proton energy content. Note that $R_{pT}=0$ by default during the NBI heating phase, including 300ms ion slowing-down time after the NBI blip.
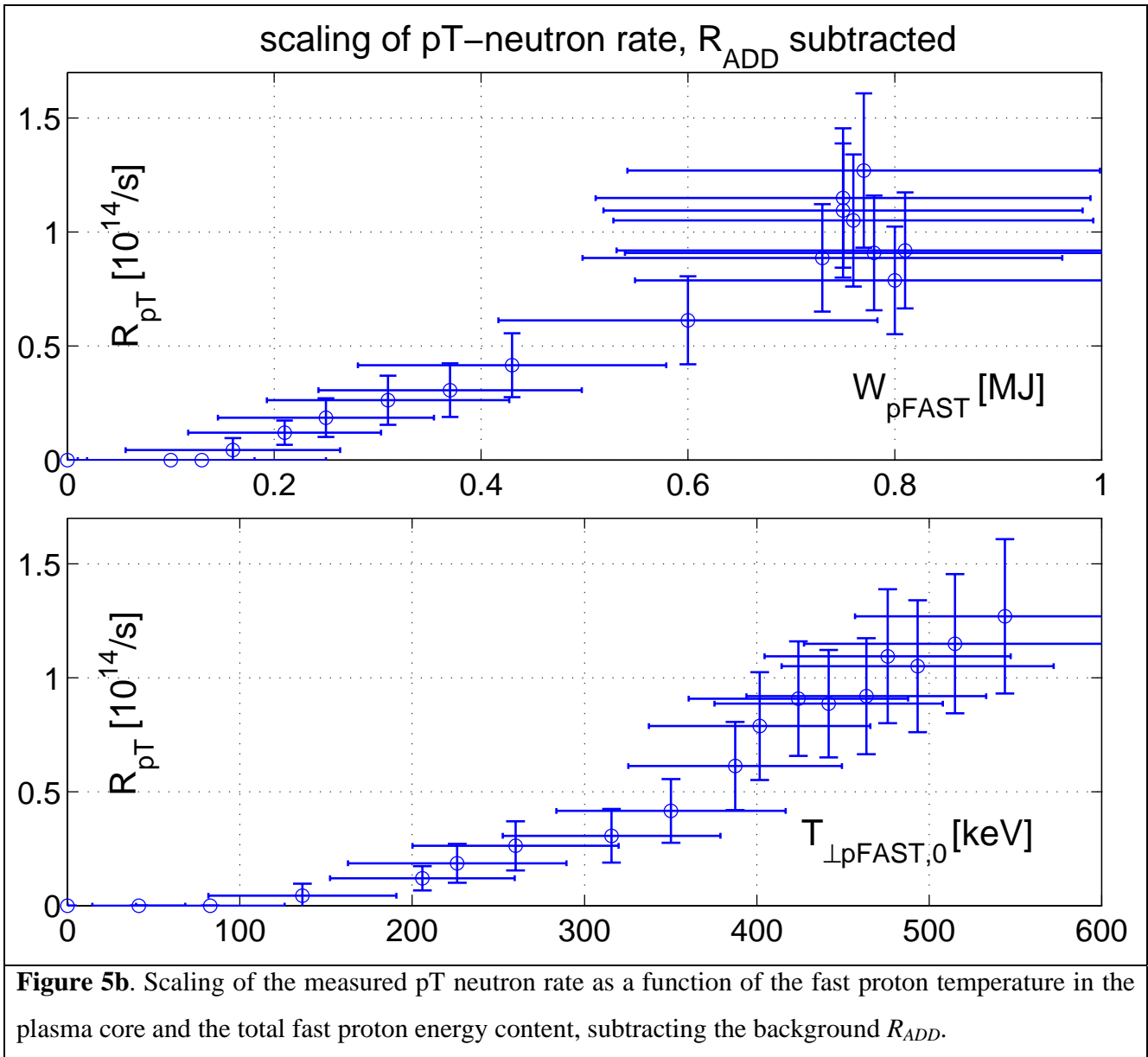
D.Testa et al., Figure 4b

}

Figure 5a. Scaling of the measured pT neutron rate as a function of the fast proton temperature in the plasma core and the total fast proton energy content. Also shown are the calculated values using three different models for the distribution function of the high energy protons: the bi-Maxwellian model is given in Eq.(3), and the pitch-angle average model is given in Eq.(5).

D.Testa et al., Figure 5a

Figure 5b. Scaling of the measured pT neutron rate as a function of the fast proton temperature in the plasma core and the total fast proton energy content, subtracting the background R_{ADD}.

D.Testa et al., Figure5b